Materials Chemistry and Physics 229 (2019) 39–48

Contents lists available at ScienceDirect

Materials Chemistry and Physics

journal homepage: www.elsevier.com/locate/matchemphys

Investigation of the structural, magnetic and dielectric properties of Mn-doped $Bi_2Fe_4O_9$ produced by reverse chemical co-precipitation

M. Pooladi[a], H. Shokrollahi[a,*], S.A.N.H. Lavasani[b], H. Yang[c]

[a] Electroceramics Group, Materials Science and Engineering Department, Shiraz University of Technology, Shiraz, Iran
[b] Faculty of Metallurgical and Materials Engineering, Semnan University, Semnan, Iran
[c] School of Science, Lanzhou University of Technology, Lanzhou, 730050, China

HIGHLIGHTS

- The aim of the work is to prepare $Bi_2Fe_{4-x}Mn_xO_9$ ferrite nanoparticles.
- The used method was the reverse co-precipitation route.
- The amount of Mn cation was changed.
- The dielectric constant and magnetic coercivity were enhanced.

ARTICLE INFO

Keywords:
Bismuth ferrite $Bi_2Fe_4O_9$
Reverse co-precipitation
X-ray diffraction

ABSTRACT

The nanoparticles of $Bi_2Fe_{4-x}Mn_xO_9$ ($0.0 \leq x \leq 1.0$) were synthesized using the reverse chemical co-precipitation method. The structural and microstructural studies of the synthesized powders were investigated by the X-ray diffractometery (XRD), Fourier-transformed infrared spectroscopy (FTIR) and field emission scanning electron microscopy (FESEM), transmission electron microscopy (TEM) and X-ray photoelectron spectrometer (XPS). The magnetic properties of nanoparticles were measured by a Vibrating Sample Magnetometer (VSM). The dielectric properties of the sintered samples were tested by the inductance-capacitance-resistance (LCR) meter equipment. The structural studies confirm the formation of the single phase of bismuth ferrite without impurities in all compositions. Microstructural observations showed that no significant changes occur in the size and shape of particles by increasing the manganese content. The produced nanoparticles are angular and pseudo-cubic-shaped and the average particle size in each sample is about 130 nm. The magnetic measurement revealed that as the Mn content increases, the coercivity increases noticeably and the saturation magnetization decreases slightly. Also, the dielectric constant was enhanced due to the Mn addition.

1. Introduction

Materials called multiferroics have the main ferroic arrangement simultaneously in the same phase like ferroelectricity and ferromagnetism [1]. One of the most attractive features of multiferroics is magneto-electric coupling [2]. The coupling of magnetism and ferroelectricity in such materials causes significant functional applications in spintronic devices, magnetoelectric memories, gas sensors and catalyst materials [3–5]. Perovskite-type bismuth ferrite ($BiFeO_3$) is the most known multiferroic material, which has been widely studied in recent decades [5,6]. In bismuth-based compounds such as $BiFeO_3$, $BiMnO_3$ and $BiCrO_3$ the structure, magnetic and ferroelectric features do not overlap so commonly and there is a weak coupling between their magnetic and ferroelectric properties, although most of the Bi-based materials are proper ferroelectrics with high magnetic and ferroelectric transition temperatures. Also, $BiFeO_3$ has a spiral spin structure on the microscopic scale near room temperature and shows very weak magnetization [7,8]. Perhaps, in this field, the discovery of a new class of multiferroics is the most exciting discussion topic, in which ferroelectricity is merely related to the magnetic arrangement and is based on it. Mullite-type Bismuth ferrite $Bi_2Fe_4O_9$ (hereafter is abbreviated as BFO) belongs to the Type2 multiferroics that contain both ferroelectric and antiferromagnetic (AFM) orders near room temperature [7]. Bismuth ferrite is a multifunctional material which has received much attention due to this feature along with the sensory and photocatalytic properties of the material and its vast potential applications [9–11]. Bismuth

* Corresponding author. Electroceramics Group, Materials Science and Engineering Department, Shiraz University of Technology, Modarres Blvd., Shiraz, Iran.
E-mail address: shokrollahi@sutech.ac.ir (H. Shokrollahi).

https://doi.org/10.1016/j.matchemphys.2019.02.076
Received 3 July 2018; Received in revised form 19 January 2019; Accepted 18 February 2019
Available online 21 February 2019
0254-0584/

ferrite $Bi_2Fe_4O_9$ is a member of the mullite family with the orthorhombic crystal structure (pbam spatial group) and the lattice parameters of a = 7.905 Å, b = 8.428 Å and c = 6.005 Å [11]. In such structures, Fe atoms are placed at two different octahedral (Fe^{3+}- O_6) and tetrahedral (Fe^{3+} - O_4) sites. There is a ferromagnetic coupling between each Fe spin cation in the octahedral position. Besides, there is an antiferromagnetic coupling between each Fe spin cation in the tetrahedral position with the similar spin direction and with the Fe spin cation in octahedral. The mutual interaction between them causes a spin frustration which leads to creating antiferromagnetic ordering in this structure [12,13]. Many chemical methods such as the solid-state precursor method, sol-gel routes and hydrothermal process have been used to produce the pure phase BF [14–16]. The material properties strongly depend on the structural and microstructural properties, as well as synthesis method [3]. Chemical co-precipitation due to its significant benefits like the simple processing, easy controlling of conditions and suitable particle size range has found its place in the field of nanotechnology and wet chemical synthesis. This method is regarded as a kind of pH change during the procedure and is divided into different types such as normal and reverse methods. On the other hand, a recent study in the field of $BiFeO_3$ synthetization using normal and reverse chemical co-precipitation shows that the normal method is an inefficient procedure in preparing $BiFeO_3$ due to the non-conservative stoichiometric ratio during the precipitation reactions [17]. Whereas the cationic and basic solutions in the synthetization of $BiFeO_3$ and $Bi_2Fe_4O_9$ via chemical co-precipitation are the same, we have chosen the reverse chemical co-precipitation to prepare the BF powders. Hence, in the current study, the reverse chemical co-precipitation method is used as a result of its ability to control the morphology and structure of doped-BF [18]. This technique provides an economical and simple method suitable for the synthesis of nano-scaled multiferroic ceramics. Several attempts have been made to improve the magnetic and ferroelectric properties of BF by substituting ions like Sc, Al, Zr, and Co [19–22]. To the best of our knowledge, these properties have not yet been investigated for Mn-doped BF. The aim of this paper is to prepare $Bi_2Fe_{4-x}Mn_xO_9$ (BFM) ferrite nanoparticles using a reverse co-precipitation method and to focus on the impact of manganese on the structural, magnetic and electrical properties.

2. Materials and methods

2.1. Synthesis procedure

Pure-phase and Mn-doped $Bi_2Fe_4O_9$ powders were prepared using the reverse chemical co-precipitation synthesis technique. In a typical procedure, the chemical reagents, namely high-purity analytical grade iron nitrate nonahydrate $Fe(NO_3)_3{\cdot}9H_2O$ (Merck 98%), bismuth subnitrate $Bi_5H_9N_4O_{22}$ (Sigma-Aldrich 98%), manganese nitrate tetrahydrate $Mn(NO_3)_2{\cdot}4H_2O$ (Merck 98%), nitric acid HNO_3 (Merck 65%) and sodium hydroxide NaOH (Merck 98%) were utilized as raw materials without any further purification. Iron nitrate was dissolved in deionized water, and bismuth subnitrate was dissolved in 2 N nitric acid (HNO_3) for 0.2 N Fe^{3+} and Bi^{3+} solutions. These solutions were mixed and stirred at the stoichiometric molar ratio (Table 1) for 40 min to obtain a homogeneous transparent mixture. 1.5 N sodium hydroxide (NaOH) was used as a precipitating agent. Afterward the cations solution was vented into the separator funnel and the precipitating agent was loaded into the glass beaker. Then the cations solution was added drop by drop into the precipitating agent while the stirrer was working severely to obtain the pH value of 9. The chemical co-precipitation process lasted about 15 min and after the entire precipitation, the suspension was stirred for another 3 min for homogenization. Then the suspension was filtered and washed several times with distilled water until the pH value reached 7. Subsequently, the precipitate was dried in the air atmosphere for 5 days and then the dried chunks were ground in a mortar. At last for crystallization and phase formation, the powders were calcined at 750 °C in alumina crucibles and air atmosphere for 60 min at the 10 °C/min heating rate. The abbreviations of the samples with different percentages of manganese 0.00, 0.05, 0.10, 0.15, 0.20 and 0.25 were named BF, BF5, BF10, BF15, BF20 and BF25, respectively (Table 1).

Table 1
Abbreviated symbols of samples with different amount of dopants.

Sample abbreviation	Manganese percentage	Stoichiometric molar ratio Bi:Fe:Mn	Chemical Formula
BF	0.00	1.00:2.00:0.00	$Bi_2Fe_4O_9$
BF5	0.05	1.00:1.90:0.10	$Bi_2Fe_{3.8}Mn_{0.2}O_9$
BF10	0.10	1.00:1.80:0.20	$Bi_2Fe_{3.6}Mn_{0.4}O_9$
BF15	0.15	1.00:1.70:0.30	$Bi_2Fe_{3.4}Mn_{0.6}O_9$
BF20	0.20	1.00:1.60:0.40	$Bi_2Fe_{3.2}Mn_{0.8}O_9$
BF25	0.25	1.00:1.50:0.50	$Bi_2Fe_3MnO_9$

2.2. Characterization

All tests were performed at the temperature of the surrounding environment. The crystalline structure of the calcined nanopowders was examined by an X-ray diffractometer (Philips X'Pert-MPD Model) using the Cu-Kα radiation and the scan rate 0.05°/min in the scattering angular range (2θ) of 10–90°. The crystallite size (D) of the nanoparticles was determined using the Scherer equation $D(hkl) = 0.91\lambda/B\cos\theta$ where λ is the Cu-Kα wavelength (0.154 nm); B is the full width at half maximum (FWHM, radian); and θ is the Bragg angle. Fourier transformed infrared studies using a spectrometer (FT-IR, Perkin Elemer RX1) in the range of 400–4000 cm^{-1} were recorded. The specimens were prepared using the KBr medium. A field emission scanning electron microscope (FESEM, MIRA3-TESCAN) was employed to examine the microstructure, morphology, and elemental composition of nanopowders. The FESEM was equipped with X-ray energy dispersive spectroscopy (EDXS). The microstructure of nanopowders was investigated by transmission electron microscopy (TEM, JEM-1200EX). The electron binding energies and valence states of all elements were characterized by an X-ray photoelectron spectrometer (XPS, PHI-5702). The magnetic characterization of the obtained powder samples were measured using a vibration sample magnetometer (VSM, JDAW-2000D) with a maximum magnetic field of 15 kOe. The relative dielectric constant (ε′) and loss tangent (tan δ) at the frequency of 1000 Hz–1 MHz were measured by using the inductance–capacitance–Resistance meters (LCR meter, HP/4284A).

3. Results and discussion

3.1. FT-IR spectroscopy

In order to investigate the chemical structures and bounding, the FTIR analysis in the wavelength range of 400–4000 cm^{-1} was performed on the samples of BF, BF15 and BF25 before and after the heat treatment. Before the heat treatment, the samples had an amorphous structure and contained nitrate compounds, hydrates and some water which is due to the precursors used at the synthesis stage. In Fig. 1(a), there are two absorption bands at wavelengths 3424 and 1624 cm^{-1}, which are, respectively, related to the stretching vibration of the −OH and H−O−H of the water molecules. The absorption bands at 1327 and 845 cm^{-1} are due to the remaining nitrates (−NO_3) from the preparation process and the absorption band at 1466 cm^{-1} is related to metal hydroxides. Hence, according to the precursor used in the synthesis, it is related to Bismuth and Iron hydroxides ($Bi(OH)_3$ and $Fe(OH)_3$) [23]. The absorption band at 1064 cm^{-1} is related to the stretching vibrations of the Mn^{3+}- O band [24]. After the heat treatment of the samples, there are no absorption bands for organic compounds (−OH, −H−O−H, and −NO_3) in the diagram (Fig. 1(b)). This is probably due to the heat

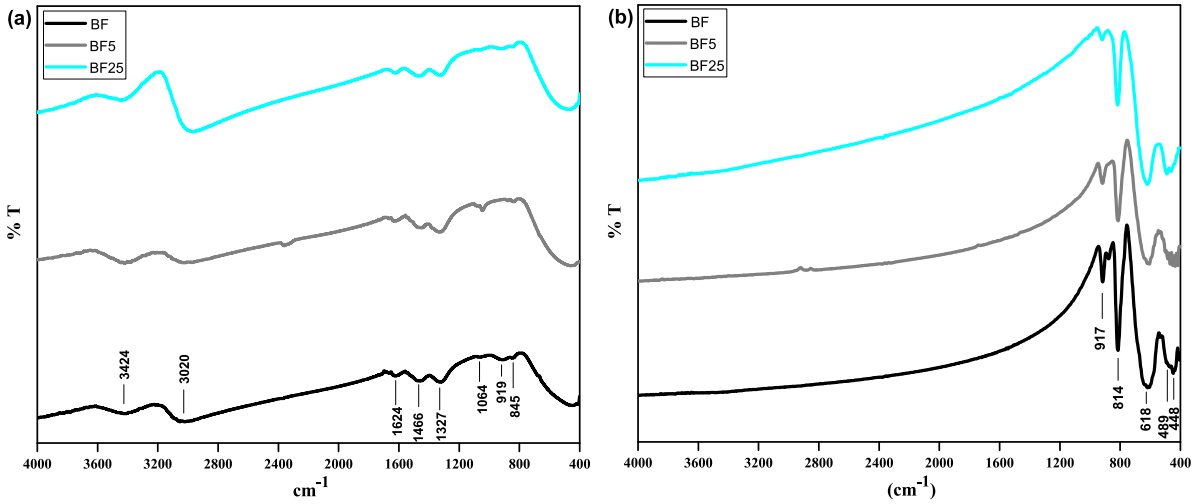

Fig. 1. FT-IR data of (a) precursors samples of BF, BF15 and BF25 (b) calcined samples of BF, BF15 and BF25 at 750 °C.

treatment process since the bands in organic compounds are destroyed by the evaporation of the remaining water in the particles and the decomposition of nitrates and hydrates. In ferrites, the absorption bands in the range 400–900 cm^{-1} are related to the stretching vibrations of tetrahedral and octahedral complexes. The absorption band at 489 cm^{-1} is related to the bending vibrations of the O—Fe—O at the tetrahedral sites. At the wavelength 618 cm^{-1}, the absorption band is simultaneously associated with the bending vibration of Fe—O—Fe in the tetrahedral position (FeO_4) and the vibrations of Bi—O band at the octahedral site (BiO_6). The two absorption bands at 448 and 814 cm^{-1} are related to the stretching vibrations of Fe—O in the octahedral position and the stretching vibrations of the Fe—O at the tetrahedral site, respectively [25]. The absorption peak at around 900 cm^{-1} is likely related to the bonding between A-site and B-site. In this case, it can be related to the bonding of Bi—Fe, as well as Bi—Mn. All the bands shown in Fig. 1(a) and (b) confirm the successful synthesis of bismuth ferrite $Bi_2Fe_4O_9$ using the reverse co-precipitation method. Additionally, the good placement of iron cations at the tetrahedral (FeO_4) and octahedral (FeO_6) sites has been shown [26].

3.2. XRD analysis

Fig. 2 shows XRD the patterns of the undoped $Bi_2Fe_4O_9$ and Mn^{2+} doped $Bi_2Fe_{4-x}Mn_xO_9$ (where X = 0.05, 0.1, 0.15,0.20 & 0.25) powders, which were synthesized using the reverse co-precipitation method at a

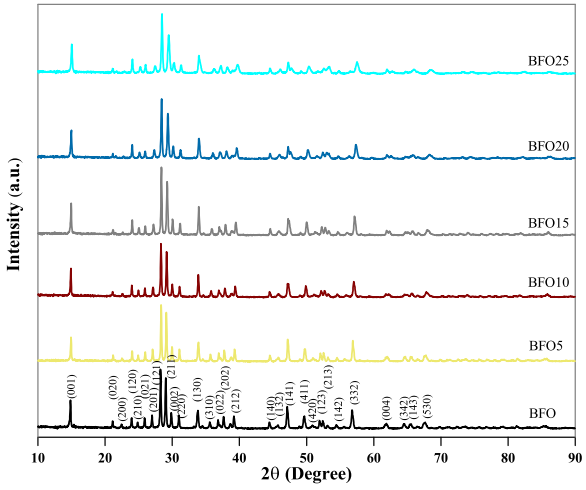

Fig. 2. X-ray diffraction patterns of all samples.

constant pH value of 9 and calcined at 750 °C for 1 h. Patterns are reviewed, indicating the single-phase formation of orthorhombic $Bi_2Fe_4O_9$ with the space group pbam No.55. Additionally, the crystalline structure is constant and remains unchanged in the all samples. The analysis of X-ray diffraction patterns for all samples confirms the formation of the single-phase BF and BFM for the pure bismuth ferrite and the bismuth ferrite with an additional percentage of manganese, respectively. According to the results obtained from the XRD patterns, there are no undesired phases, such as Fe_2O_3, Bi_2O_3 and $BiFeO_3$ in all samples that can be detected in the sensitivity range of the given device. The absence of impurities, namely Fe_2O_3 and Bi_2O_3 indicates the appropriate selection of the co-precipitation synthesis type. It is noteworthy that the type of co-precipitation, i.e. the reverse co-precipitation plays a great role in this regard. The formation of the $BiFeO_3$ phase as a byproduct along with $Bi_2Fe_4O_9$ is almost common during the heat treatment process, especially when the mole percentage of the additive element is greater than 10%, this issue has been reported in similar studies that used the additives of Sc and La [19,27]. In this research, the absence of the $BiFeO_3$ phase even in the samples with high percentages of manganese (BF20, BF25) is a remarkable point.

The enlarged X-ray patterns in the 2θ range of 26–32° have been shown in Fig. 3. By increasing the percentage of manganese (Mn^{2+} in Fe^{3+} site), the peaks shift towards the right-hand and larger angles. From the theoretical perspective, according to Bragg's Law (Eq. (1)) and the formula for orthorhombic crystal lattices (Eq. (2)), the peaks shifting toward the right reduce the distance between crystalline planes (d) and consequently reduce lattice parameters. It would be worth mentioning that in the following equations, λ is the Cu-Kα wavelength (0.154 nm); d is the interplanar spacing; θ is the Bragg angle; n is equal to 1; h, k, l are the Miller indices and a, b, c are the lattice parameters. The lattice parameters a, b, and c are calculated for all samples using Rietveld analysis and the crystallite size (D) of the nanoparticles was determined using the Scherer equation $D(hkl) = 0.91\,\lambda/B\cos\theta$. The obtained results in Table 2 indicate the slight changes in parameters a and c where both parameters show a decreasing trend by increasing the manganese percentage.

By increasing the amount of manganese in the lattice, the unit cell volume significantly decreased linearly. A decrease in the unit cell volume can be due to the differences in the ion size and the site preference of different ions Fe^{3+}, Mn^{3+}, and Mn^{4+}. This may cause an incomplete transformation of cation Mn^{2+} (0.97 Å) with a cationic radius greater than Fe^{3+} (0.785 Å) in the lattice, some of them may appear in the form of cations Mn^{3+} (0.72 Å) with the site preferences of tetrahedron and, to some extent, Mn^{4+} (0.67 Å) with the site preferences of octahedron, and due to their smaller cationic radius than the

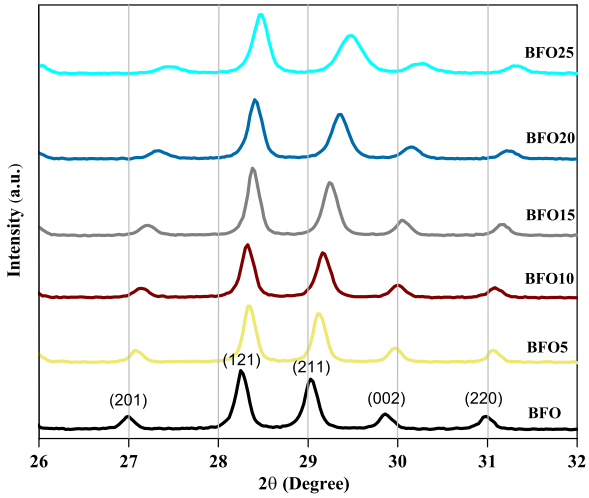

Fig. 3. The magnified X-ray diffraction patterns of all samples.

$$n\lambda = 2dsin\theta \quad (1)$$

$$\frac{1}{d^2} = \frac{h^2}{a^2} + \frac{k^2}{b^2} + \frac{l^2}{c^2} \quad (2)$$

Table 2
Structural parameters of the pure phase BF and BFM samples.

Sample	'a' (Å)	'b' (Å)	'c' (Å)	Cell Volume (Å^3)	Crystallite Size (nm)
BF	7.944	8.441	5.997	402.130	54
BF5	7.932	8.431	5.985	400.245	63
BF10	7.894	8.434	5.967	397.720	55
BF15	7.879	8.425	5.962	395.760	54
BF20	7.829	8.427	5.938	391.759	40
BF25	7.798	8.434	5.921	389.414	29

Fe^{3+} cationic radius, both tend to reduce the lattice parameters, resulting in a decrease in the unit cell volume [28–31]. The obvious changes in the unit cell volume of the lattice confirm the successful manganese substitution into the $Bi_2Fe_4O_9$ lattice.

3.3. Microstructural observation

In order to perform the microstructural and morphological analysis, the field emission scanning electron microscopy was carried out on the bismuth ferrite powder samples with different percentages of Mn-doped (x = 0, 0.05, 0.10, 0.15, 0.20 and 0.25). In Fig. 4 the pure bismuth ferrite (BF) sample shows that the produced nanoparticles are angular and pseudo-cubic-shaped. According to our findings, no significant changes occur in the size and shape of particles when manganese is added and by increasing the manganese percentage, the average particle size in each sample is about approximately 130 nm.

The difference between our particle sizes and crystallite sizes (Table 2) means that the achieved nanoparticles are the polycrystalline and that there are several grains in each particle. The powder morphology shows that the produced compounds are in the form of agglomerates and that the particle size distribution is almost uniform. For samples with a high percentage of manganese, the particle agglomeration is slightly decreased. The nature of co-precipitation synthesis method affects the particle size distribution and the particle agglomeration. In the chemical co-precipitation synthesis, the pH of the reaction environment is always variable, which is the most important factor affecting the particle size [3,19]. The crystal growth rate is higher in some directions due to the presence of the relatively extreme crystallographic growth direction preference and the high percentage of Bi atoms with high diffusion rates [32]. Thus, the formation of angular particles, especially the cubic-shaped is justifiable. For the $Bi_2Fe_4O_9$ compound with the mullite crystal structure, when the manganese is selected as an additive element, it can be completely placed at the substitutional sites [28]. This is justified by the fact that $Bi_2Mn_4O_{10}$ also has the mullite crystal structure and its manganese is placed at the tetrahedral and square pyramidal sites [30,33]. Consequently, by adding manganese to $Bi_2Fe_4O_9$, this element is rejected by the crystalline structure to a very small extent, which has no significant effect on the particle growth. The distribution of particle size for all samples was measured and with the user error of ± 8 nm shown in Fig. 5.

As can be seen from Fig. 5, the number of particles in the medium range in case of high amounts of additives was increased. In order to determine the distribution, the atomic/weight percentage of the constituent elements of the synthesized substance, the Energy Dispersive X-ray Spectroscopy (EDS) and the surface analysis were performed on the as-sintered BF20 sample at 820 °C. The sintered BF20 sample was used in two different regions to examine the distribution of elements. The colors blue, green, red and yellow are related to Fe, Mn, Bi and O, respectively. Fig. 6(a) indicates the perfect uniform and ideal distribution of all elements over the sample surface and the cross-section view of the tablet (sample) has been shown. Fig. 6(b) shows the inner center of the tablet, where the elements of Mn and Fe are more uniformly distributed than those of Bi and O.

Another objective of this test is to investing ate the presence of undesirable elements such as Na (for as much as the Na ions are present in the precipitant solution, it was possible that they remain after the washing and calcination). As it is clear, the compositional elements are limited to Bi, Fe, Mn and O. In order to provide further insight results into the morphology, particle size distribution and growth orientation of produced samples in more detail, the as-selected sample BF20 was investigated by TEM and HRTEM. These micrographs of $Bi_2Fe_4O_9$ nanoparticles have been shown in Fig. 7.

According to Fig. 7(a), it is obvious that the average particle size is approximately about 150 nm with a suitable distribution in the range of 60–210 nm and that the agglomerated morphology due to the fast precipitation reaction during the reverse co-precipitation process and high surface energy of nanoparticles can clearly be observed. Also, the particles have the pseudo-spherical and cubic shapes, which were seen by FESEM micrographs (Fig. 4). Fig. 7(b) depicts the HRTEM micrograph of BF20. The orderly arrays of faces indicate the single-crystalline nature of the nanoparticles. The lattice spacing of an individual nanoparticle are 0.41 and 0.59 nm, corresponding to the crystal planes of (020), (001) of orthorhombic $Bi_2Fe_4O_9$, respectively. This data demonstrates that the basal plane of this nanoparticle has the [100] crystal zone axis.

3.4. XPS studies

The XPS analysis was used for BF5 and BF20 samples in order to determine the elemental oxidation states in ceramics. Fig. 8(a) shows the XPS spectra of Bi 4f consisting of two sharp peaks at 158.7 eV and 164.0 eV corresponding to the binding energy of Bi $4f_{7/2}$ and $4f_{5/2}$, respectively [34]. This implies the existence of the Bi^{3+} valence state in the both samples. By comparing the Bi 4f spectra of two samples, the lack of change in Bi 4f binding energy is clearly understood by increasing the amount of manganese. The Fe 2p spectra contain two peaks of Fe $2p_{3/2}$ and Fe $2p_{1/2}$, as shown in Fig. 8(b). The binding energy of the Fe $2p_{3/2}$ peak is fitted into two main peaks. The position of these peaks for BF5 is at 710.0 eV and 711.5 eV, resulting from the Fe^{2+} and Fe^{3+} oxidation state of iron. The Fe $2p_{3/2}$ peak has associated two satellite peaks in the range 713.3 eV and the 718.6 corresponds to Fe^{2+} and Fe^{3+} respectively [35–38]. As shown in Fig. 8(b), the results from the BF20 sample are similar to the BF5 sample This connotes that Fe is present in the two oxidation states of +2 and + 3 in the BFM phase. Fig. 8(c) shows the O 1s XPS spectra. It is found that the O 1s spectra can be fitted with two peaks. The peak at 529.6 eV is assigned to the

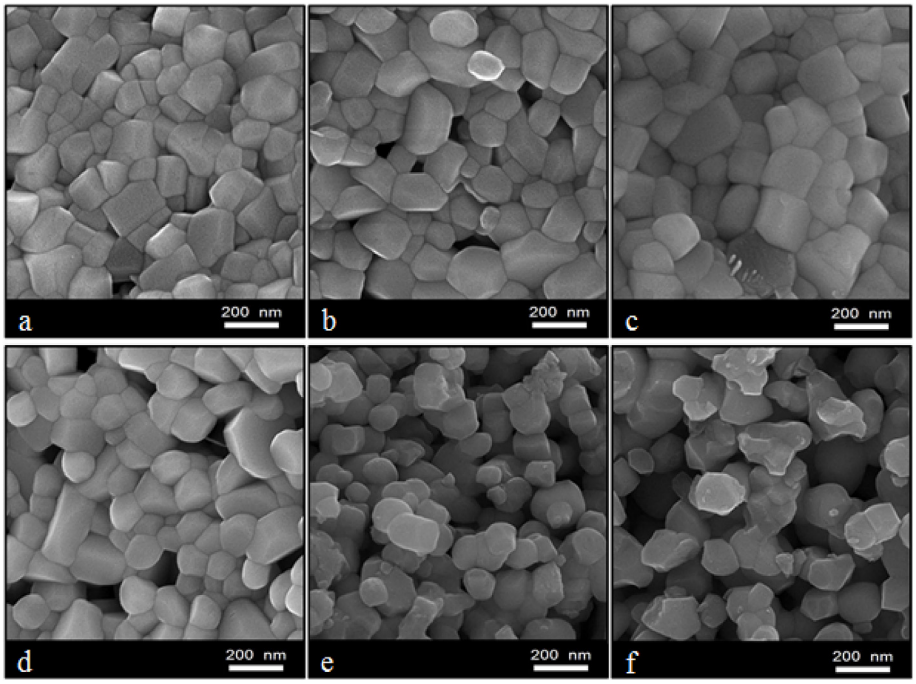

Fig. 4. FESEM micrographs of (a) BF, (b) BF5, (c) BF10, (d) BF15, (e) BF20, (F) BF25 samples.

crystal lattice oxygen (O_L) and the peak at 531.3 eV is attributed to the presence of oxygen vacancies (O_V) in the ceramics [35]. It seems that by increasing the amount of manganese (BF20), oxygen vacancy increases slightly. Also, oxygen vacancy can indicate the present of Fe^{2+} oxidation states. On the Mn 2p XPS spectra (Fig. 8(d)), the analysis of the Mn 2p XPS spectra for BF5 sample is indiscernible due to the large background. But for BF20 sample, the Mn $2p_{3/2}$ peak is at 642.1 eV and is attributed to Mn^{3+} oxidation state. The other peak at 644.7 eV and the satellite peaks at 648.5 eV correspond to the core level of Mn^{4+} oxidation state in the ceramics [39–41].

3.5. Magnetic evaluation

Bismuth ferrite BF is an antiferromagnetic substance; however, it exhibits a weak ferromagnetic behavior due to the remnant magnetic moments on the surface of the substance, leading to the incomplete neutralization of the magnetic moments [42,43]. Nanocrystals of $Bi_2Fe_4O_9$ ferrite shows not only antiferromagnetic order of Fe^{3+} moments but also weak ferromagnetism. In the tetrahedral site (FeO_4), Fe^{3+} moments couple antiferromagnetically among themselves and with the octahedral (FeO_6) Fe^{3+} moments and there is a ferromagnetic ordering within a pair of octahedral Fe^{3+} spins [42]. As a result, the Fe^{3+} cations exhibit Cairo pentagonal lattices and consequently non-collinear magnetic structure [44].

The magnetic hysteresis loops at room temperature were measured for pure BF and Mn-doped BFM samples. The obtained results have been portrayed in Fig. 9 and Table 3. At low amounts of Mn addition, the magnetization decreases due to the tendency of Fe^{3+} to remain in higher spin states (5 μ_B per Fe^{3+}), the presence of high amounts of Mn^{2+} with the moment of 5 μ_B, the increase in crystallite sizes. Zhang et al. show the magnetization decreases with increasing the crystallite size. They also found a transition from antiferromagnetism to weak ferromagnetism occurs when the average diameter becomes below 57 nm [45].

With increasing the Mn content from its initial value, the concentration of Mn^{3+} and Mn^{4+} and also the lattice distortion (distortion of Fe−O tetrahedra and octahedral) will be increased. Difference in magnetic moment of Mn^{3+}, Mn^{4+} with Fe^{3+} cations suppresses canted spin structure resulting in increase of magnetization. Furthermore, this substitution with different valence and radius of cations can damage the balance between the anti-parallel site magnetization of Fe^{3+} ions. The substitution of Mn^{3+} and Mn^{4+} ions with low magnetic moments compared to the Mn^{2+} suppresses or breaks the spiral spin structure. This effect leads to the breakdown of balance between the antiparallel sublattice magnetization of Fe^{3+} a distorted crystal field on iron ions and consequently a noncompletely quenched orbital magnetic moment. This coupling forms a spin-orbital interaction [46]. This type of coupling introduces the magnetic anisotropy on the iron lattice sites and then suppresses the spiral spin ordering, resulting in the increase of magnetization.

The BF20 sample exhibits the weak ferromagnetic behavior to some extent, which is due to the lack of oxygen anions (due to the presence of cations with strong positive centers) and a little partial strain of the lattice in case of large amounts of additives. In the BF25, the sample shows a greater tendency to antiferromagnetic behavior, which can be due to the angled spins that lead to some remnant magnetization. The substitution of cations Mn^{3+} (L = 2, S = 2, J = 0) and Mn^{4+} (L = 3/2, S = 3/2, J = 3/2) with none-zero angular momentum (L ≠ 0) instead of the cation Fe^{3+} (L = 0, S = 5/2, J = 5/2) with zero angular momentum increases the spin-orbit-lattice coupling and the magnetic anisotropy is significantly high when the amounts of manganese in samples BFO20 and BFO25 are high (Table 3).

3.6. Dielectric properties

Fig. 10(a) and (b) show the changes in the relative dielectric constant (ε') and the dielectric loss tangent ($\tan\delta$) with respect to the frequency at the temperature of the surrounding environment. The linear behavior of changes in the dielectric constant at high frequencies is clearly visible for all samples.

At low frequencies, the dielectric constant is reduced monotonously, while it remains fixed at high frequencies and its changes have a linear behavior. Based on the Maxwell–Wagner polarization mechanism, the lack of oxygen and lattice defects (grain boundaries and dislocations) leads to the electric heterogeneity in the sample, which is a reason for polarization at low frequencies. At frequencies higher than the intrinsic

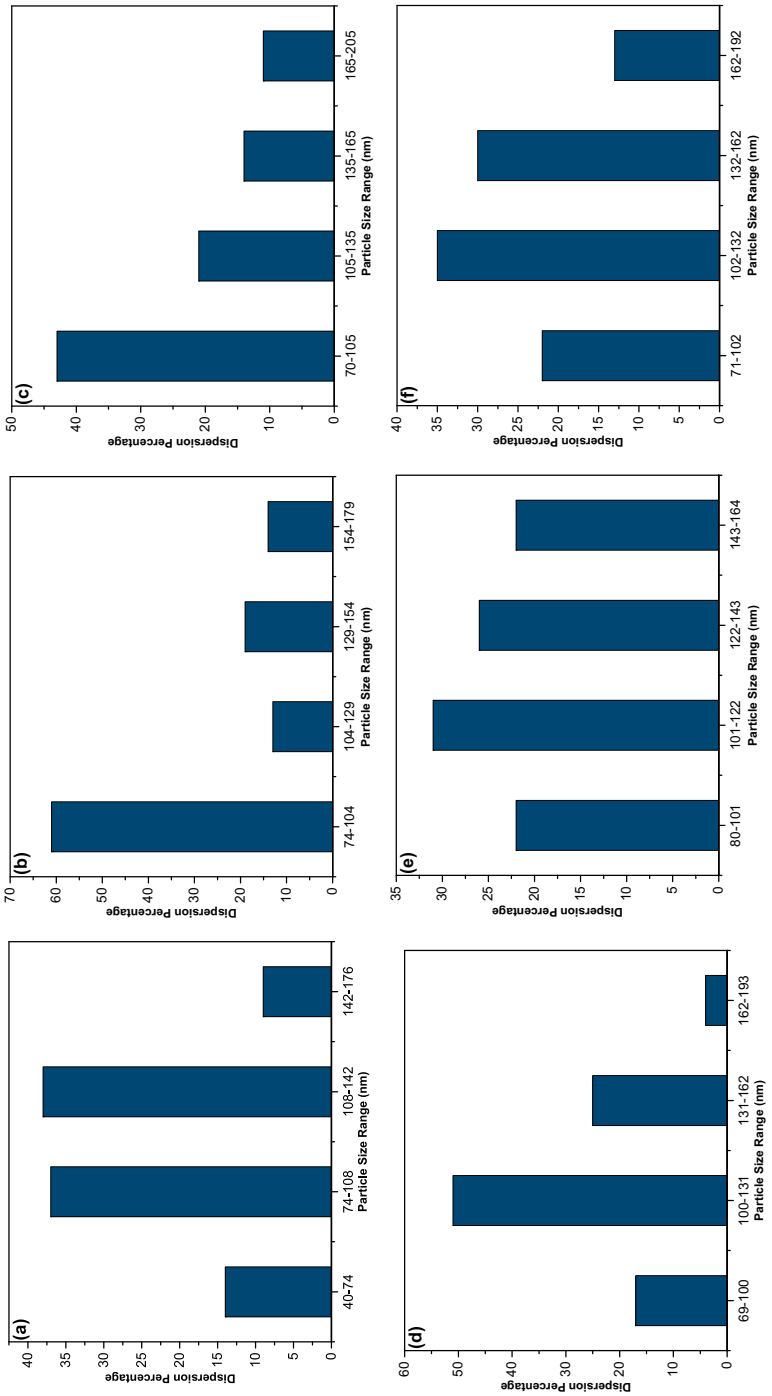

Fig. 5. The particle size distribution of (a) BF, (b) BF5, (c) BF10, (d) BF15, (e) BF20, (F) BF25 samples.

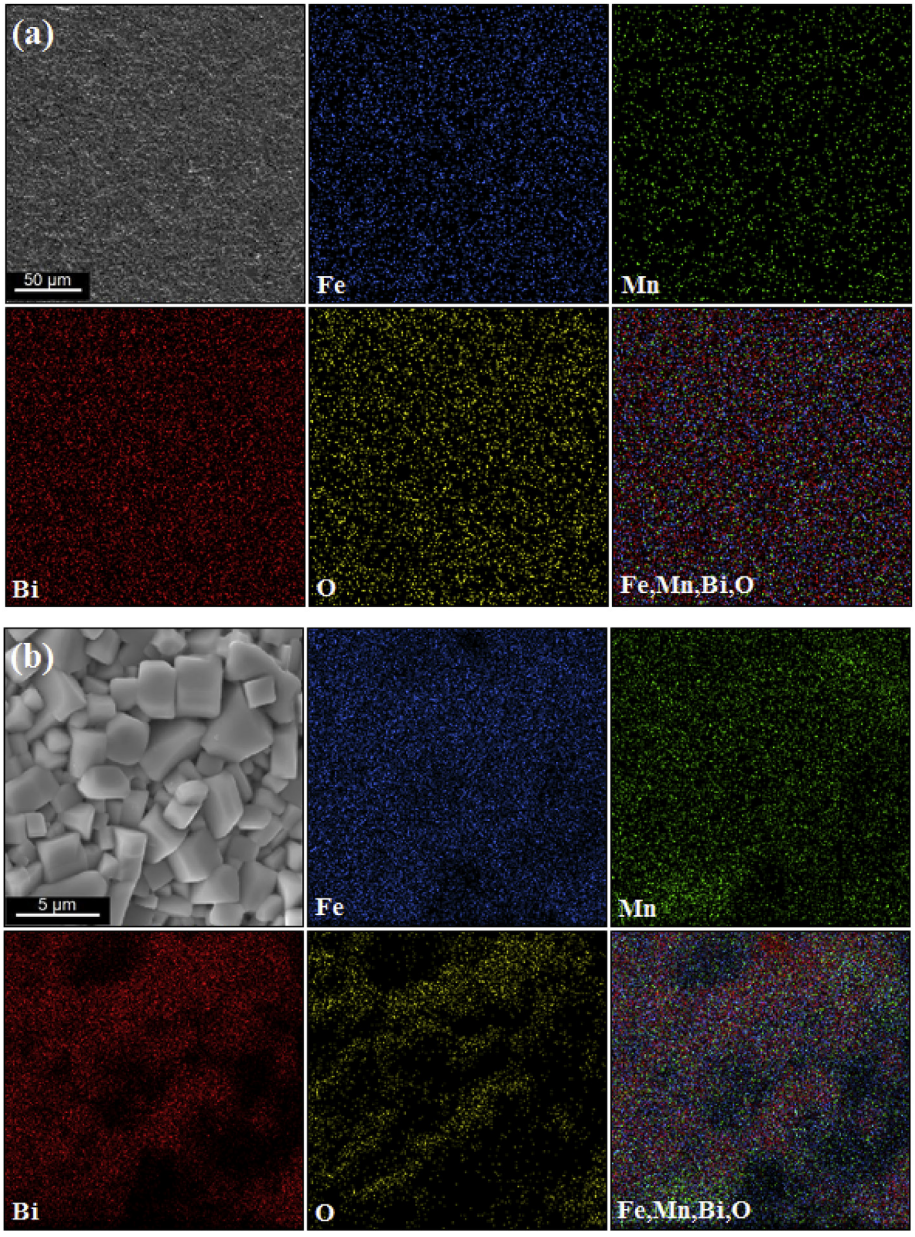

Fig. 6. Surface analysis (map) of (a) cross-section of as-synthesized BF20 bulk sample (b) center of BF20 bulk sample.

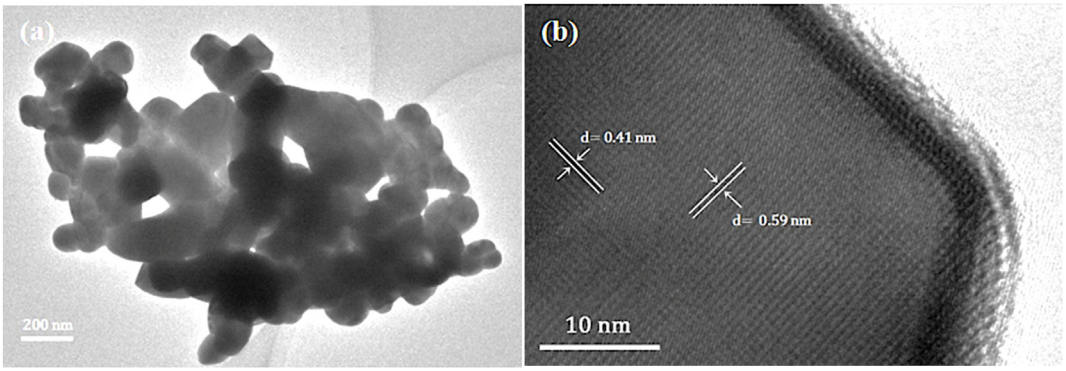

Fig. 7. Transmission electron microscopy of as-selected BF20 sample, (a) TEM micrograph of an agglomerated nanoparticles and (b) HRTEM micrograph of an individual nanoparticle.

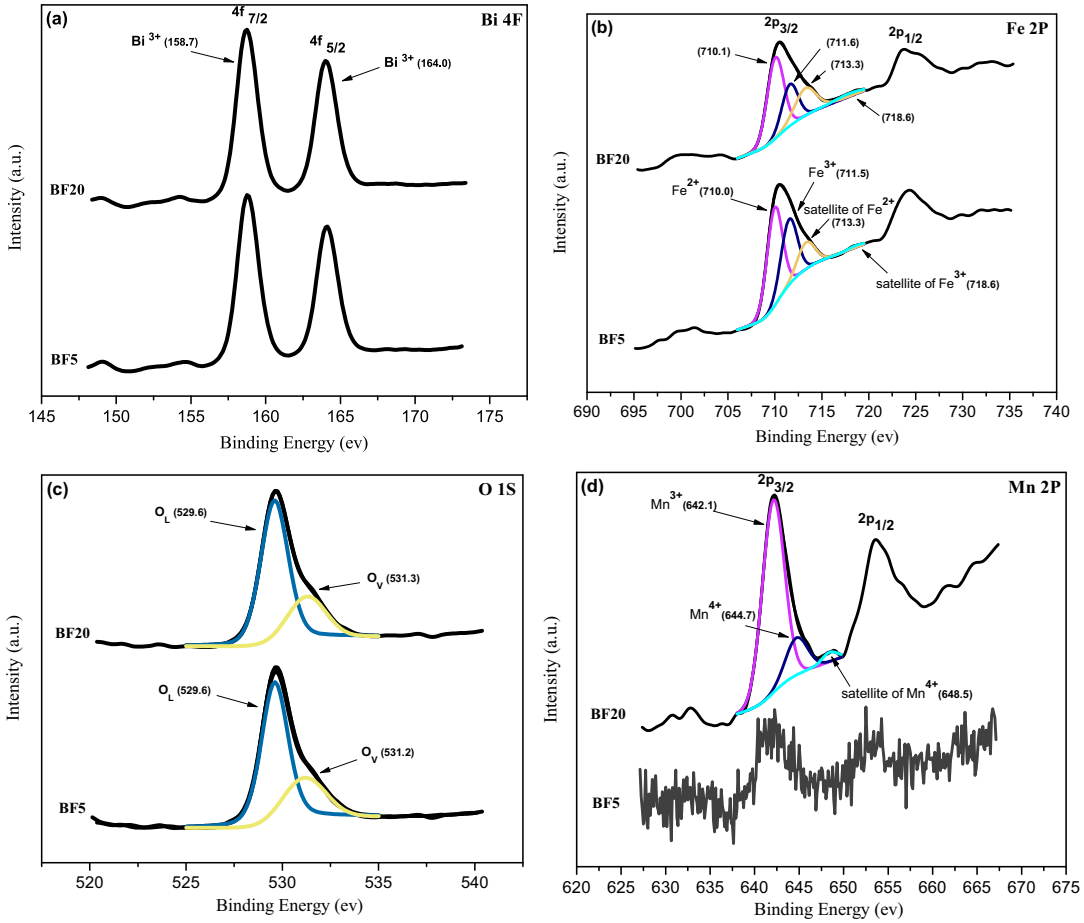

Fig. 8. XPS spectra of as-selected BF5 and BF20 samples. (a) Bi 4f XPS spectra; (b) Fe 2p XPS spectra; (c) O 1s XPS spectra; (d) Mn 2p XPS spectra.

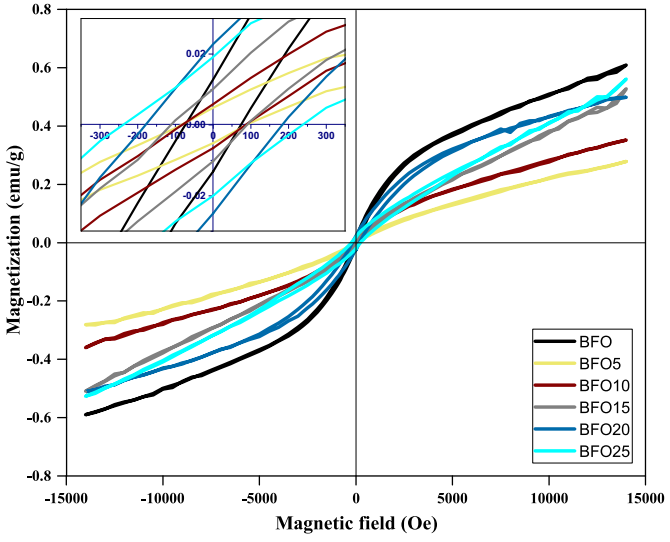

Fig. 9. Magnetization versus applied magnetic field (M-H loops) of powder samples.

resonance frequency of the substance, the dielectric cannot interact with the applied frequency and therefore the electric dipole response to the frequency will necessarily be delayed. The reason is that the electric dipole (space charges) is not able to follow the applied field and that the changes in the applied frequency are faster than the dielectric relaxation time [47,48]. In Fig. 10(a) an increase in the relative dielectric constant, especially at low frequencies may be due to an increase in the

Table 3
Magnetic parameters of the pure phase BF and BFM samples.

Sample	Magnetization at 15000 Oe (emu/g)	M_r (emu/g)	H_c (Oe)
BF	0.609	0.013	74.11
BF5	0.319	0.005	73.95
BF10	0.439	0.006	83.75
BF15	0.502	0.010	129.85
BF20	0.440	0.023	182.80
BF25	0.560	0.019	238.87

fluctuation space of the oxygen octahedron. Additionally, the dielectric loss decreases by increasing the frequency. At relatively low frequencies, the accumulation of space charges on the surface and at interphase interfaces leads to high losses, which indicates the polarization of the space charge. The accumulation of charge at high frequencies decreases and consequently reduces losses.

The doping Mn ions dependence of the relative dielectric constant (ε′) and dielectric loss tangent (tan δ) for $Bi_2Fe_{4-x}Mn_xO_9$ ($0 \le X \le 1$) nanoparticles has been shown in Fig. 10(a) and (b). At different frequencies, the dielectric constant and the dielectric loss tangent show a steady increase by increasing the Mn doping. In ferrites, the electron transfer or electron hopping ($Fe^{3+} + e \leftrightarrow Fe^{2+}$) between two ions ferric (Fe^{3+}) and ferrous (Fe^{2+}) results in the frequency-dependent polarization and the energy required for electron hopping from one cation to another one is called the activation energy [49]. As previously mentioned, it is most likely that the manganese ion appears in different oxidation states in the composition, including double, triple and quadruple. Therefore, the electron transfer can be formulated through the following charge compensation equations:

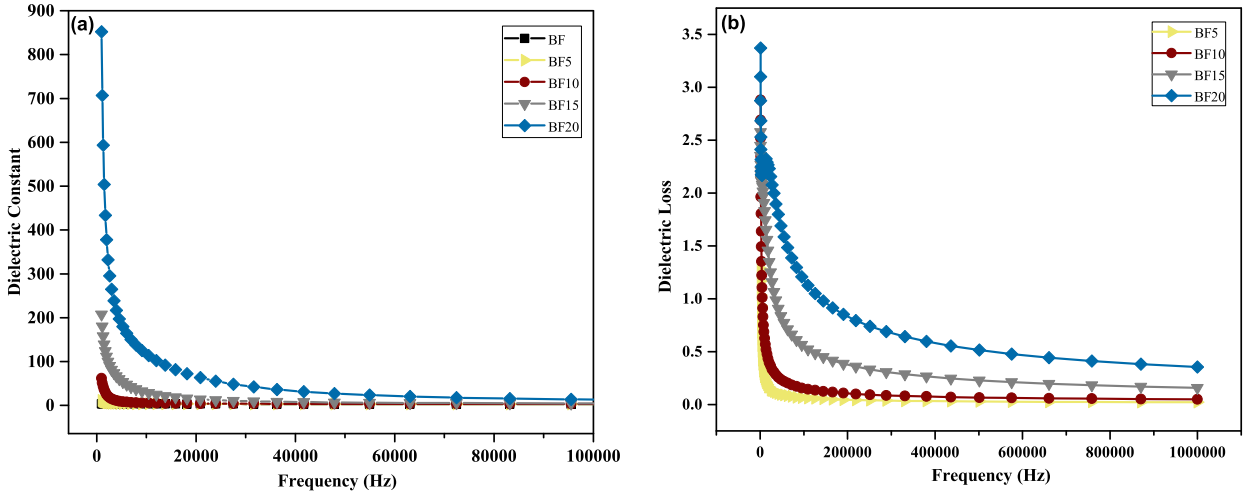

Fig. 10. (a) Dielectric constant vs. frequency and (b) dielectric loss vs. frequency, of BF and BFM ceramics at room temperature.

$$Fe^{3+} + Mn^{3+} \leftrightarrow Fe^{2+} + Mn^{4+} \quad (3)$$

$$Fe^{3+} + Mn^{2+} \leftrightarrow Fe^{2+} + Mn^{3+} \quad (4)$$

By increasing the amount of Mn ions, more energy is needed for electron hopping from one cation to another, which reduces the conductivity and increases the dielectric constant. In other words, in order to form Mn 3d-O 2p hybridization, Mn ions occupy the Fe^{3+} site and lie in the oxygen octahedron. Therefore, the improved ferroelectric properties are achieved due to the enhanced stabilization of the ferroelectric distortion. Similar results have been reported for the Mn doping of $EuFeO_3$ ceramics by sultan et al. [50].

4. Conclusion

In this study, the mullite-type bismuth ferrite powder with different percentages of Mn-doping (x = 0, 0.05, 0.10, 0.15, 0.20 and 0.25) was synthesized by a reverse chemical co-precipitation method. The effect of manganese doping on the structural, magnetic and electrical properties of ferrite was investigated. Based on the results of XRD and FTIR, the synthesis using the reverse co-precipitation method was successful and there was no impurity in compounds with different percentages of manganese. Additionally, the results of XRD showed that by increasing the percentage of manganese ion in the ferrite, the unit cell volume of lattice is significantly decreased. Given the fact that the substituted Mn^{2+} ions have a higher cationic radius than Fe^{3+} ions, the decrease is likely due to the appearance of manganese ions in various oxidation states (Mn^{2+}, Mn^{3+}, Mn^{4+}). According to FESEM observations, there were no significant changes in the shape and size of particles by adding manganese to ferrite. The analysis results from TEM observations, the produced nanoparticles are angular and pseudo-cubic-shaped, and the average particle size is about 130 nm. XPS analyses illuminate that Mn is present in the two oxidation states of +3 and + 4 in the BFM phase. It seems that the presence of Mn^{3+} and Mn^{4+} cations has an influence on the magnetic properties. The reduction of magnetization in the case of low amounts of additives and the significant increase of H_c in the case of high amounts of additives is heavily dependent on the presence of these two cations. Finally, by adding manganese to ferrite, the dielectric constant of the sintered samples is increased, thereby improving the dielectric properties of ferrites.

Appendix A. Supplementary data

Supplementary data to this article can be found online at https://doi.org/10.1016/j.matchemphys.2019.02.076.

References

[1] H. Schmid, Some symmetry aspects of ferroics and single phase multiferroics, J. Phys. Condens. Matter 20 (2008) 434201.
[2] W. Eerenstein, N. Mathur, J.F. Scott, Multiferroic and magnetoelectric materials, Nature 442 (2006) 759–765.
[3] R. Safi, H. Shokrollahi, Physics, chemistry and synthesis methods of nanostructured bismuth ferrite (BiFeO3) as a ferroelectro-magnetic material, Prog. Solid State Chem. 40 (2012) 6–15.
[4] R. Köferstein, T. Buttlar, S.G. Ebbinghaus, Investigations on Bi25FeO40 powders synthesized by hydrothermal and combustion-like processes, J. Solid State Chem. 217 (2014) 50–56.
[5] G. Catalan, J.F. Scott, Physics and applications of bismuth ferrite, Adv. Mater. 21 (2009) 2463–2485.
[6] J. Wang, J. Neaton, H. Zheng, V. Nagarajan, S. Ogale, B. Liu, D. Viehland, V. Vaithyanathan, D. Schlom, U. Waghmare, Epitaxial BiFeO3 multiferroic thin film heterostructures, Science 299 (2003) 1719–1722.
[7] D. Khomskii, Classifying multiferroics: mechanisms and effects, Physics 2 (2003) 20.
[8] I. Sosnovska, T. Peterlin-Neumaier, E. Steichele, Spiral magnetic ordering in bismuth ferrite, J. Phys. 15 (1982) 4835–4846.
[9] A. Poghossian, H. Abovian, P. Avakian, S. Mkrtchian, V. Haroutunian, Bismuth ferrites: new materials for semiconductor gas sensors, Sensor. Actuator. B Chem. 4 (1991) 545–549.
[10] L.J. Di, H. Yang, T. Xian, X.J. Chen, Construction of Z-scheme g-C3N4/CNT/Bi2Fe4O9 composites with improved simulated-sunlight photocatalytic activity for the dye degradation, Micromachines 9 (2018) 613.
[11] L. Di, H. Yang, T. Xian, X. Chen, Enhanced photocatalytic activity of NaBH4 reduced BiFeO3 nanoparticles for rhodamine B decolorization, Materials 10 (2017) 1118.
[12] N. Niizeki, M. Wachi, The crystal structures of Bi2Mn4O10, Bi2Al4O9 and Bi2Fe4O9, Z. für Krist.-Cryst. Mater. 127 (1968) 173–187.
[13] E. Ressouche, V. Simonet, B. Canals, M. Gospodinov, V. Skumryev, Magnetic frustration in an iron-based Cairo pentagonal lattice, Phys. Rev. Lett. 103 (2009) 267204.
[14] Z. Pchelkina, S. Streltsov, Ab initio investigation of the exchange interactions in Bi2Fe4O9: the Cairo pentagonal lattice compound, Phys. Rev. B 88 (2013) 054424.
[15] Y. Wang, G. Xu, L. Yang, Z. Ren, X. Wei, W. Weng, P. Du, G. Shen, G. Han, Low temperature synthesis of Bi2Fe4O9 nanoparticles via a hydrothermal method, Ceram. Int. 35 (2009) 51–53.
[16] T. Liu, Y. Xu, C. Zeng, Synthesis of Bi2Fe4O9 via PVA sol–gel route, Mater. Sci. Eng. B 176 (2011) 535–539.
[17] L. Wang, J. Li, J.-B. Xu, A.-M. Chang, L. Bian, B. Gao, K.-T. Liu, Bi2Fe4O9 submicron-rods synthesized by a low-heating temperature solid state precursor method, J. Alloy. Comp. 562 (2013) 64–68.
[18] H. Sangian, O. Mirzaee, M. Tajally, S.A.N.H. Lavasani, Monitoring the Bi/Fe ratio at different pH values in BiFeO3 nanoparticles derived by normal and reverse chemical co-precipitation: a comparative study on the purity, microstructure and magnetic properties, Ceram. Int. 44 (2018) 5109–5115.
[19] S.A.N.H. Lavasani, O. Mirzaee, H. Shokrollahi, A.K. Moghadam, M. Salami, Magnetic and morphological characterization of Bi2Fe4O9 nanoparticles synthesized via a new reverse chemical co-precipitation method, Ceram. Int. 43 (2017) 12120–12125.
[20] D.P. Dutta, C. Sudakar, P.S.V. Mocherla, B.P. Mandal, O.D. Jayakumar, A.K. Tyagi, Enhanced magnetic and ferroelectric properties in scandium doped nano Bi2Fe4O9, Mater. Chem. Phys. 135 (2012) 998–1004.
[21] S. Huang, L.R. Shi, Z.M. Tian, S.L. Yuan, C.M. Zhu, G.S. Gong, Y. Qiu, Effect of Al3+ substitution on the structural, magnetic, and electric properties in multiferroic Bi2Fe4O9 ceramics, J. Solid State Chem. 227 (2015) 79–86.
[22] G. Wang, S. Nie, J. Sun, S. Wang, Q. Deng, Effects of Zr4+ doping on structure,

magnetic and optical properties of Bi2Fe4O9 powders, J. Mater. Sci. Mater. Electron. 27 (2016) 9417–9422.
[23] S. Mohapatra, B. Sahu, M. Chandrasekhar, P. Kumar, S. Kaushik, S. Rath, A. Singh, Effect of cobalt substitution on structural, impedance, ferroelectric and magnetic properties of multiferroic Bi2Fe4O9 ceramics, Ceram. Int. 42 (2016) 12352–12360.
[24] M. Kong, H. Song, F. li, D. Dai, H. Gao, Facil synthesis of Bi2Fe4O9 nanoplateand its application as a novel adsorbent for Cu (II) removal, J. Environ. Chem. Eng. 5 (2017) 69–78.
[25] R. Chen, W. Xiao, Hierarchically porous MnO2 microspheres with enhanced adsorption performance, J. Mater. Chem. 1 (2013) 11682–11690.
[26] Z. Hu, B. Chen, T. Lim, Single-crystalline Bi2Fe4O9 synthesized by low-temperature co-precipitation: performance as photo- and Fenton catalysts, J. RSC Adv. 4 (2014) 27820–27829.
[27] J.H. Miao, T.T. Fang, H.Y. Chung, C.W. Yang, Effect of La doping on the phase conversion, microstructure change, and electrical properties of Bi2Fe4O9 ceramics, J. Am. Ceram. Soc. 92 (2009) 2762–2764.
[28] Z.R. Kann, J.T. Auletta, E.W. Hearn, S.U. Weber, K.D. Becker, H. Schneider, M.W. Lufaso, Mixed crystal formation and structural studies in the Mullite-type system Bi2Fe4O9 – Bi2Mn4O9, J. Solid State Chem. 185 (2012) 62–71.
[29] D.M. Giaquinta, H.-C. zur Loye, Synthesis and structure of Bi2Fe2Mn2O10, J. Alloys. Compd. 184 (1992) 151–160.
[30] N. Nguyen, M. Legrain, A. Ducouret, B. Raveau, Distribution of Mn3+ and Mn4+ species between octahedral and square pyramidal sites in Bi2Mn4O9 - type structure, J. Mater. Chem. 9 (1999) 731–734.
[31] A. Ianculescu, F.P. Gheorghiu, P. Postolache, O. Oprea, L. Mitoseriu, The role of doping on the structural and functional properties of BiFe1-xMnxO3 magnetoelectric ceramics, J. Alloy. Comp. 504 (2010) 420–426.
[32] M.S. Bernardo, T. Jardiel, M. Peiteado, A.C. Caballero, M. Villegas, Reaction pathways in the solid state synthesis of multiferroic BiFeO3, J. Eur. Ceram. Soc. 31 (2011) 3047–3053.
[33] P.E. Kalita, A.L. Cornelius, K.E. Lipinska, M.W. Lufaso, Z.R. Kann, S. Sinogeikin, O.A. Hemmers, H. Schneider, New pressure induced phase transitions in mullite-type Bi2(Fe4-xMnx)O10-δ complex oxides, Int. J. Mater. Res. 103 (2012) 464–468.
[34] C.X. Zheng, H. Yang, Assembly of Ag3PO4 nanoparticles on rose flower-like Bi2WO6 hierarchical architectures for achieving high photocatalytic performance, J. Mater. Sci. Mater. Electron. 29 (2018) 9291–9300.
[35] X.X. Zhao, H. Yang, S.H. Li, Z.M. Cui, C.R. Zhang, Synthesis and theoretical study of large-sized Bi4Ti3O12 square nanosheets with high photocatalytic activity, Mater. Res. Bull. 107 (2018) 180–188.
[36] Y.X. Yan, H. Yang, X.X. Zhao, R.S. Li, X.X. Wang, Enhanced photocatalytic activity of surface disorder-engineered CaTiO3, Mater. Res. Bull. 105 (2018) 286–290.
[37] Y.C. Ye, H. Yang, H. Zhang, J. Jiang, A Promising Ag2CrO4/LaFeO3 Heterojunction Photocatalyst Applied to Photo-Fenton Degradation of RhB, Environmental technology, 2018, https://doi.org/10.1080/09593330.2018.1538261.
[38] X. Wen, Z. Chen, E. Liu, X. Lin, X.,C. Chen, Effect of Ba and Mn doping on microstructure and multiferroic properties of BiFeO3 ceramics, J. Alloy. Comp. 678 (2016) 511–517.
[39] S.J. Lee, S. Gavriilidis, Q.A. Pankhurst, A. Kyek, F.E. Wagner, P.C. Wong, K.L. Yeung, Effect of drying conditions of Au–Mn co-precipitates for low-temperature CO oxidation, J. Catal. 200 (2001) 298–308.
[40] J.S. Foord, R.B. Jackman, G.C. Allen, An X-ray photoelectron spectroscopic investigation of the oxidation of manganese, Philos. Mag. A 49 (1984) 657–663.
[41] M.C. Biesinger, P.B. Payne, A.P. Grosvenor, L.W. Lau, A.R. Gerson, R.S.C. Smart, Resolving surface chemical states in XPS analysis of first row transition metals, oxides and hydroxides: Cr, Mn, Fe, Co and Ni, Appl. Surf. Sci. 257 (2011) 2717–2730.
[42] J.T. Han, Y.H. Huang, R.J. Jia, G.C. Shan, R.Q. Guo, W. Huang, Synthesis and magnetic property of submicron Bi2Fe4O9, J. Cryst. Growth 294 (2006) 469–473.
[43] M. Liu, H. Yang, Y. Lin, Y. Yang, Influence of Co doping on the magnetic properties of Bi2Fe4O9 powders, J. Mater. Sci. Mater. Electron. 25 (2014) 4949–4953.
[44] S. Huang, L.R. Shi, Z.M. Tian, S.L. Yuan, C.M. Zhu, G.S. Gong, Y. Qiu, Effect of Al3+ substitution on the structural, magnetic, and electric properties in multiferroic Bi2Fe4O9 ceramics, J. Solid State Chem. 227 (2015) 79–86.
[45] Qiang Zhang, Wenjie Gong, Jiaheng Wang, Xinkun Ning, Zhenhua Wang, Xinguo Zhao, Weijun Ren, Zhidong Zhang, Size-dependent magnetic, photoabsorbing, and photocatalytic properties of single-crystalline Bi2Fe4O9 semiconductor nanocrystals, J. Phys. Chem. C 115 (2011) 25241–25246.
[46] Miao Liu, Haibo Yang, Ying Lin, Yanyan Yang, Influence of Co doping on the magnetic properties of Bi2Fe4O9 powders, J. Mater. Sci. Mater. Electron. 25 (2014) 4949–4953.
[47] K.W. Wagner, The distribution of relaxation times in typical dielectrics, Ann. Phys. 40 (1973) 817–819.
[48] A.K. Jonscher, Dielectric Relaxation in Solids, MI, Chelsea Dielectric Press, London, 1983, p. 335.
[49] M.d. Amir, B. Ünal, S.E. Shirsath, M. Geleri, M. Sertkol, A. Baykal, Polyol synthesis of Mn3+ substituted Fe3O4 nanoparticles: cation distribution, structural and electrical properties, Superlattice. Microst. 85 (2015) 747–760.
[50] K. Sultan, M. Ikram, K. Asokan, Effect of Mn doping on structural, morphological and dielectric properties of EuFeO3 ceramics, RSC Adv. 5 (2015) 93867–93876.